Spontaneous Conformational Changes in the *E. coli* GroEL Subunit from All-Atom Molecular Dynamics Simulations

Yelena Sliozberg and Cameron F. Abrams
Department of Chemical and Biological Engineering, Drexel University, Philadelphia, Pennsylvania

ABSTRACT The *Escherichia coli* chaperonin GroEL is a complex of identical subunit proteins (57 kDa each) arranged in a back-to-back stacking of two heptameric rings. Its hallmarks include nested positive intra-ring and negative inter-ring cooperativity in adenosine trisphosphate (ATP) binding and the ability to mediate the folding of newly transcribed and/or denatured substrate proteins. We performed unbiased molecular dynamics simulations of the GroEL subunit protein in explicit water both with and without the nucleotide KMgATP to understand better the details of the structural transitions that enable these behaviors. Placing KMgATP in the equatorial domain binding pocket of a **t** state subunit, which corresponds to a low ATP-affinity state, produced a short-lived (6 ns) state that spontaneously transitioned to the high ATP-affinity **r** state. The important feature of this transition is a large-scale rotation of the intermediate domain's helix M to close the ATP binding pocket. Pivoting of helix M is accompanied by counterclockwise rotation and slight deformation of the apical domain, important for lowering the affinity for substrate protein. Aligning simulation conformations into model heptamer rings demonstrates that the **t**→**r** transition in one subunit is not sterically hindered by **t** state neighbors, but requires breakage of Arg^{197}-Glu^{386} intersubunit salt bridges, which are important for inter-ring positive cooperativity. Lowest-frequency quasi-harmonic modes of vibration computed pre- and post-transition clearly show that natural vibrations facilitate the transition. Finally, we propose a novel mechanism for inter-ring cooperativity in ATP binding inspired by the observation of spontaneous insertion of the side chain of Ala^{480} into the empty nucleotide pocket.

INTRODUCTION

Chaperonins are protein complexes that mediate in vivo protein folding by consuming adenosine trisphosphate (ATP). GroEL/GroES, an essential chaperonin to *E. coli* and responsible for successful production of >10% of the organism's proteome, is the most comprehensively studied chaperonin system (1,2). GroEL is a cylindrical homotetradecamer in which the subunits (57 kDa each) are arranged in a back-to-back stacking of two rings of seven subunits each (3,4) (Fig. 1, *a* and *b*), and its co-chaperonin GroES is a homoheptamer of smaller subunits (10 kDa each) (5). A single ring can bind seven molecules of ATP and at least one substrate polypeptide. GroEL functions by switching heptamer ring ligand affinities in an alternating manner between rings. In the **T** state, a ring has low nucleotide and high substrate peptide affinities, while in the **R** state, these are reversed. The **T**→**R** transition occurs in an essentially concerted manner among all seven subunits (i.e., a $\mathbf{t}_7 \rightarrow \mathbf{r}_7$ transition) upon positively cooperative binding of seven molecules of ATP (6,7). Because of negative cooperativity between the rings, the adjoining ring simultaneously undergoes a transition in the opposite direction (8), normally resulting in ejection of hydrolysis product adenosine diphosphate (ADP) and, if present, co-chaperonin GroES. A ring cavity can bind a nascent or misfolded substrate protein in the **T** state (9) and eject it by transitioning to the **R** state. Binding of GroES transitions the **R**-state ring to the **R**″ state, forming a cage (10) into which polypeptide is ejected and left to fold without potentially aggregation-inducing interactions (11). The irreversibility of ATP hydrolysis ultimately drives the directionality of GroEL/ES function.

Although a complete understanding of the structural basis of GroEL function remains elusive, it necessarily involves large relative motion of three distinct domains of the subunit protein (12):

1. The large equatorial domain, labeled *E* in Fig. 1 *c*, is comprised of residues 2–136 and 411–526, contains all inter-ring and most intra-ring contacts as well as both the N and C termini of the protein, and contributes the majority of residues of the nucleotide binding site (13).
2. The relatively less structured apical domain (A), residues 192–375, presents hydrophobic patches to which both co-chaperonin GroES and unfolded substrate polypeptides can bind (14).
3. The intermediate domain (I), residues 137–191 and 376–410, connects the equatorial the apical domains.

A subunit transitions from low (**t**) to high (**r**) ATP affinity when the intermediate domain closes down over the nucleotide binding pocket (15), accompanied by a small counterclockwise rotation of the apical domain in the plane of the ring (viewed from above) (16). (Lowercase letters ***t*** and ***r*** refer to the subunit tertiary structural states in the heptamer allosteric states ***T*** and ***R***, respectively.) In transitioning from **r** to **r**″, the intermediate domain remains closed over the nucleotide, but the apical domain must rotate by more than 110° clockwise and 60° upward to bind the GroES subunit (10).

Submitted March 6, 2007, and accepted for publication May 10, 2007.
Address reprint requests to C. F. Abrams, E-mail: cfa22@drexel.edu.
Editor: Ivet Bahar.

0006-3495/07/09/1906/11 $2.00
doi: 10.1529/biophysj.107.108043

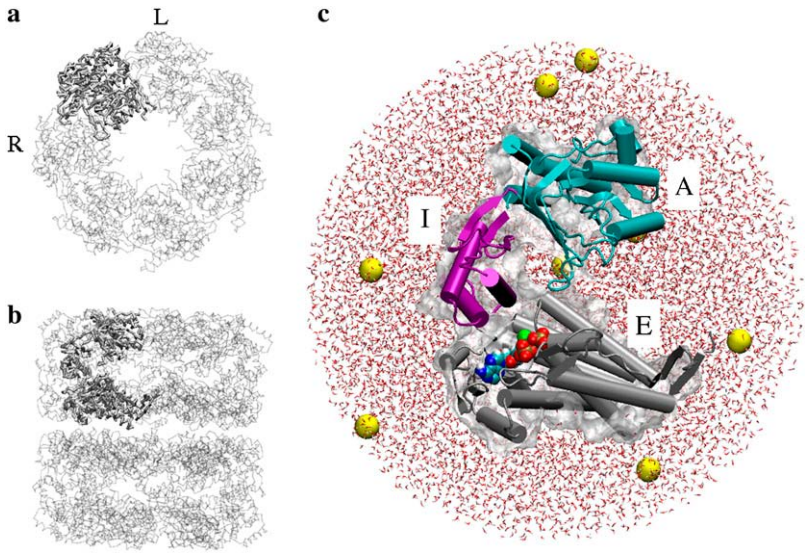

FIGURE 1 Schematic representation of construction of the simulation system for the *holo* (ATP-bound) simulation. The tetradecamer (GroEL-KMgATP)$_{14}$, from crystallographic data of Wang and Boisvert (PDB code 1KP8 (17)) in (*a*) top and (*b*) side views emphasizing a single subunit viewed from vantage point that makes domain identification clear. Left- and right-hand neighboring subunits, according to convention, are labeled in panel *a*. (c) Rendering of the simulation initial conditions: protein depicted in cartoon form with equatorial domain (*E*) in gray, intermediate (*I*) in purple, and apical (*A*) in cyan. KMgATP depicted with space-filling spheres (*cyan*, C; *blue*, N; *white*, H; *red*, O; *brown*, P; *green*, Mg; and *yellow*, K). Water represented in wireframe, together with free potassium (*yellow spheres*) with the near half clipped to prevent an obscured view of the protein. A surface shell built on the far half of protein atoms appears as a translucent surface behind the protein. The radius of the confining sphere is 56 Å and the system contains ~69,000 atoms. (This figure and others with protein renderings were produced using VMD (34,35).)

Interestingly, structural ambiguities in the **r** state subunit have proven relatively difficult to resolve compared to the **t** and **r**″ states, hampering a complete understanding of the structural bases for both positive intra-ring and negative inter-ring cooperativity. No crystal structure of an **R**-state ring exists because of difficulties preventing hydrolysis of bound ATP (17). Asymmetric **TR** tetradecamers of hydrolysis-defective mutants have been visualized using cryoelectron microscopy (16), but docking of fragments of existing atomically resolved crystal structures into electron density maps from cryo-EM neglects internal flexibility of those fragments, potentially obscuring important structural changes.

Both positive intra-ring and negative inter-ring cooperativity with respect to binding of ATP play central roles in the remarkable orchestration required to drive $\mathbf{t}_7{:}\mathbf{r}_7 \rightarrow \mathbf{r}_7{:}\mathbf{t}_7$ transitions in a nearly concerted fashion. Mediating the necessary communication of binding pocket occupancy from one subunit to both intra- and inter-ring neighbors must involve intersubunit salt bridges, because mutants without these bridges display reduced or absent cooperativity (2,18). In particular, Glu^{386} links to Arg^{197}, joining a subunit's intermediate domain to the apical domain of its counterclockwise neighbor in the ring (viewed from above), and the Arg^{197} mutant displays no positive cooperativity (18). To arrive at a complete picture of GroEL function, one must understand the mechanisms by which salt bridges communicate binding pocket occupancy among neighboring subunits. This requires understanding the dynamics involved in transitioning among the various allosteric states, since execution of such a transition reflects that an allosteric signal was properly transmitted and received.

Given both the need to predict the structure of the **r** state as well as to understand detailed transition mechanisms, molecular simulation techniques continue to provide valuable insights. The first detailed molecular model of the dynamics of the $\mathbf{t} \rightarrow \mathbf{r}''$ transition, using targeted molecular dynamics, led to the significant claim that concertedness among subunits in the transition is guaranteed by steric interactions, but also indicated that the **r** state has an apical domain rotated clockwise rather than counterclockwise (19). In a much more recent and larger-scale coarse-grained molecular modeling study of the entire $\mathbf{T} \rightarrow \mathbf{R}''$ transition, counterclockwise apical domain rotation in the $\mathbf{t} \rightarrow \mathbf{r}$ transition was enforced by using the cryo-EM structure as a target (20), and, as a result, the role of static interactions in concertedness was reduced. Both of these studies involved forcing the subunits to execute their allosteric transitions from a starting structure to a target structure in computationally feasible times using fictitious driving forces that bias motion toward the target. Although large scale, detailed, targeted dynamic simulations are able to elucidate plausible transition mechanisms, because of the fictitious nature of the driving forces, it is in principle impossible to gauge their accuracy without reference to unbiased simulations, which have been avoided primarily because of computational expense. There have been, so far, no detailed simulation studies that directly predict the $\mathbf{t} \rightarrow \mathbf{r}$ transition in the GroEL subunit based solely on an initial state with no target bias.

The purpose of this article is to report results of long (20 ns), unbiased molecular dynamics simulations of the GroEL subunit in explicit water, both with and without ATP. We report the first-ever observation of a spontaneous $\mathbf{t} \rightarrow \mathbf{r}$ transition in a molecular simulation of GroEL in the absence of target bias. In agreement with cryo-EM structures (16,21), we observe ~20° counterclockwise rotation of the apical domain along with closing of the nucleotide binding pocket. The designation of the final state reached in our simulations as **r** relies on many intrasubunit geometrical measures as well as the disposition of intersubunit salt bridges inferred from model alignments. We show that the large-scale motion

displayed in the spontaneous transition is strongly correlated with a few lowest-frequency quasi-harmonic modes of vibration. We also observe a new transition that further lowers ATP affinity and suggest a novel mechanism explaining inter-ring cooperativity based on this transition.

METHODS

We generated two 20-ns MD trajectories: one with KMgATP, designated the *holo* simulation, and one without, designated the *apo* simulation, using NAMD v2.5 (22) and the CHARMM force field (23–25). Initial coordinates for both the *holo* and *apo* forms of the subunit were taken from the crystallographic data of the $(GroEL\text{-}KMgATP)_{14}$ complex (17) (PDB code 1KP8). Although ATP is present in the binding pocket in this structure, the intermediate domain is not closed, perhaps due to crystal packing effects. For the *holo* simulation, the Mg^{2+} and K^{+} ions and six crystallographic waters were retained; these along with ATP were deleted to generate initial coordinates for the *apo* simulation. Hydrogen atoms were inserted assuming pH 7.0. Each subunit was solvated by random placement of water molecules within a sphere of radius 56 Å, maintained using harmonic boundary conditions ($k = 10$ kcal/mol/Å^2). Potassium ions were added at random locations for charge neutrality. Each system has ~69,000 atoms. No bonded constraints were used, full electrostatics were calculated every second step, and van der Waals interactions were cut off beyond 12 Å. Each system was energy-minimized via 300 cycles of conjugate-gradient optimization. MD was then run for 20 ns with a 1-fs time step. The temperature held at 37°C using a Langevin thermostat on all heavy atoms with a coupling coefficient of 5 ps^{-1}. A schematic explaining the construction of the simulation system appears in Fig. 1.

As will be detailed in the next section, our *holo* and *apo* subunits access three major tertiary states, for which we assign the following designations:

1. **a** designates the *apo* state, which we consider the final 10 ns of the *apo* simulation.
2. **t** designates the state with ATP bound with low affinity, which we take as the state accessed between 2 and 6 ns in the *holo* simulation.
3. **r** designates the ATP-bound state with the closed binding pocket, which we take as the state accessed between 10 and 20 ns in the *holo* simulation.

Using the appropriate average coordinates from the simulations, we constructed model intra-ring trimers from among various permutations of each state by aligning equatorial domain backbone α-helix atoms against those atoms in six distinct reference heptamers:

1. Either ring in $(GroEL\text{-}KMgATP)_{14}$ [1KP8 (17)];
2. Either ring in $(GroEL)_{14}$ [1XCK (26)];
3. The ring *cis* or
4. *Trans* to GroES in the ADP bullet [1AON (10)];
5. The *holo* or
6. *Apo* ring in $(GroEL\text{-}KMgATP)_7\text{-}(GroEL)_7$ [2C7E (27)].

Each trimer is labeled with a three-letter string denoting the order of the subunit tertiary states (e.g., **aaa**) when viewed transverse to the plane the ring from outside the heptamer ring. We generated the following trimers against all reference structures (averaging among all unique trimers within each reference ring): **aaa**, **ata**, **ara**, **ttt**, **trt**, and **rrr**.

C_α quasi-harmonic analysis was performed for each state (**a**, **t**, and **r**) using at least 4 ns of integration sampled at 10-ps intervals, using built-in routines in the AMBER software package (28). In standard quasi-harmonic analysis, one diagonalizes a mass-weighted cross-correlation matrix of coordinate fluctuations about a mean structure. We sought those modes whose motion contribute most strongly to the observed transitions by assigning each mode an amplitude, a_j, such that, when the average structure of some initial state is projected along mode j with this amplitude, the root-mean square deviation between the projected structure and the average structure of some other target state is minimal. For a given mode $\mathbf{y}_j$ of the initial state, this amplitude is given by

$$a_j = \frac{\sum_{i=1}^{N} \Delta\mathbf{x}_i (\mathbf{y}_j)_i}{\sum_{i=1}^{N} (\mathbf{y}_j)_i^2}, \quad (1)$$

where $\Delta\mathbf{x}_i$ is atom i's displacement in the target state relative to the initial state. From a set of modes, the mode which, when used to project the initial structure, results in the structure most similar to the target, measured by mean-squared deviation, is the ''most important mode'' in driving the transition between the initial and target structure.

RESULTS AND DISCUSSION

The t→r transition occurs spontaneously with KMgATP in the nucleotide pocket

We conducted two 20-ns MD simulations of the GroEL subunit with initially open binding pockets: the first with ATP in the pocket (*holo*) and the second without (*apo*). The first key result is a striking structural transition occurring in the *holo* simulation between 6 and 8 ns after launch. Important structural aspects of this transition in the vicinity of the binding pocket are shown in the snapshots of Fig. 2. The Asp^{155}-Arg^{395} salt bridge first ruptures spontaneously. Because this bridge anchors helix M to helix G, spanning the two strands of the intermediate domain, its rupture allows helix M (residues 386–409) to pivot around its C-terminus in response to the strong attraction between Asp^{398} and the ATP's Mg^{2+}. Simultaneously, the helices F (141–152) and G (155–169) rotate in the same direction as does M, bringing

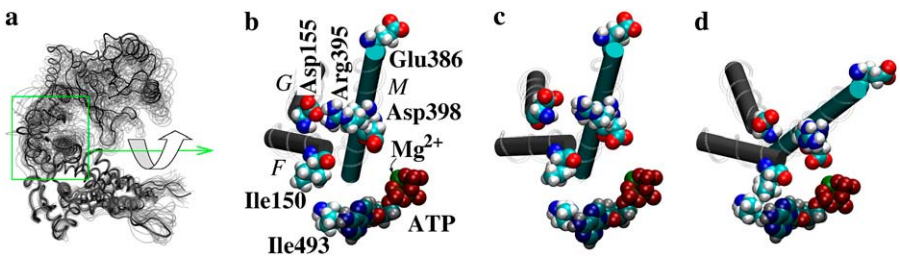

FIGURE 2 Detailed view of the **t→r** transition. (*a*) Backbone trace of the final state with transparent traces rendered every 200 ps and aligned along the equatorial domain. Remaining panels show detailed snapshots of the major structural components participating in the transition at (*b*) 3 ns, (*c*) 7 ns, and (*d*) 12 ns of simulation time, zoomed in on the region indicated by the green rectangle in panel *a*, and rotated as indicated to facilitate viewing. Helices are labeled in italics. The ATP molecule is shaded.

Ile^{150} into hydrophobic contact with Ile^{493} and ATP's adenosine, which adds another ATP-binding hydrophobic contact to the binding pocket. Gly^{492} and Leu^{494} effectively prevent the side chain of Ile^{150} from sampling the binding pocket when there is no rotation. The pivot of helix M places Asp^{398} in an H-bonded interaction with a single water molecule coordinating ATP's Mg^{2+}. This arrangement is stable for the remaining 12 ns of the total 20-ns trajectory.

The sequence of steps in the transition and their abruptness can be appreciated from Fig. 3, in which we show interatomic distance traces from the *holo* and *apo* simulations, with reference measurements from the appropriate crystal structures. The Asp^{155}-Arg^{395} salt bridge ruptures at ~6 ns, as shown by the trace of the distance between the C_γ atom of Asp^{155} and the C_ζ atom of Arg^{395} in Fig. 3 *a*. In the *holo* simulation, we see that this distance closely matches that

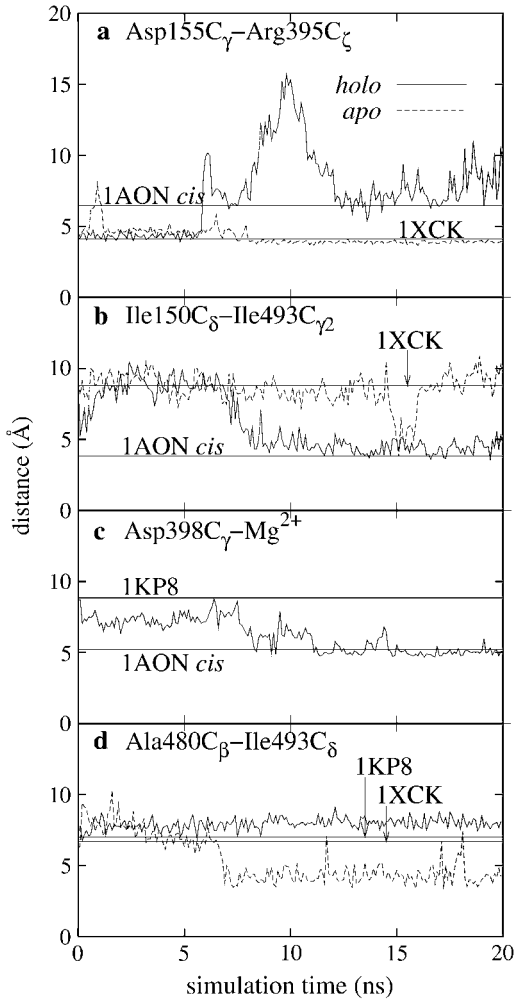

FIGURE 3 Interatomic distance traces from the MD trajectories reveal important events in the **t**→**r** (*a–c*) and Ala^{480}-insertion (*d*) transitions. Distances shown are between (*a*) C_γ of Asp^{155} and C_ζ of Arg ^{395}; (*b*) C_δ of Ile^{150} and $C_{\gamma 2}$ of Ile^{493}; (*c*) C_γ of Asp^{398} and the Mg^{2+} ion of KMgATP; and (*d*) C_β of Ala^{480} and C_δ of Ile^{493}. Horizontal lines denote measurements from reference structures indicated by their PDB accession codes (see text).

observed in the *cis* ring of the ADP-bullet crystal structure (10), which is the structure we assume as a reference displaying unambiguously closed binding pockets. We observe that, although this salt bridge breaks once early in the *apo* run, it reforms quickly and is remarkably stable for the remainder of the 20-ns simulation. This bridge is intact in all subunits of the *apo* tetradecamer (26). Next, Ile^{150} is pulled over Gly^{492} and settles into a stable hydrophobic interaction with Ile^{493} and the adenosine group of ATP after another nanosecond, as shown by the trace of the distance between the C_δ atom of Ile^{150} and the $C_{\gamma 2}$ atom of Ile^{493} in Fig. 3 *b*. This hydrophobic contact is absent in the *apo* crystal structure and present in the *cis* ring of the ADP bullet.

The force-driving motion of helix M comes from both electrostatic attraction between Mg^{2+} and the oxygens of Asp^{398} and a water-mediated hydrogen-bond network joining Mg^{2+} and Asp^{398}. There is a single water tightly coordinating the ion that donates an H-bond to an intermediate water that donates an H-bond to either oxygen of Asp^{398}. This intermediate water is not static, but this interaction site is almost always occupied by a water molecule. During the transition, this water is squeezed out and Asp^{398} accepts an H-bond from the water directly bound to the metal ion, which is thereafter a stable arrangement, as can be seen in the distance trace between the C_γ atom of Asp^{398} and Mg^{2+} in Fig. 3 *c*. After the major motion of the transition is complete, the distance between Asp^{398} and the Mg^{2+} agrees with that found in the closed binding pockets in the *cis* ring of the ADP bullet. Based on the comparison between the distance traces in Fig. 3, *a–c*, and the respective reference distances, we submit that the final state of our *holo* simulation is the **r** state.

Helices F, G, and M are the only helices in the intermediate domain, and F and M connect via different hinges directly to the equatorial domain. F and G rotate with M to maintain the hydrophobic core of the intermediate domain, but because of the distinct positions of the two hinges, the rotation involves significant internal structural rearrangement of this domain. In fact, the Asp^{155}-Arg^{395} bridge, because it anchors M to G, opposes the transition because it opposes the rearrangement that must occur to allow the rotation. This explains why the **t** state remains apparently stable for 6 ns, during which time the Asp^{155}-Arg^{395} bridge is constantly challenged by the force of attraction between Arg^{398} and Mg^{2+}. When it finally ruptures, the transition is rapid, reminiscent of uncoiling of a coiled spring. It is particularly interesting that the single underlying structural feature of GroEL that necessitates relative motion of helices G and M during the transition is that the entire protein is one giant hairpin with opposing strands in the intermediate domain with four distinct hinge points.

The Asp^{155}-Arg^{395} bridge is known to be important for positive cooperativity. In a recent study of the Asp^{155}→Ala mutant, Danziger et al. (29) showed that removing the Asp^{155}-Arg^{395} salt bridges led to a sequential rather than

concerted **T→R** transition. Our simulation shows that Asp^{155}-Arg^{395} exerts a force on helix M that is opposed by Asp^{398}-Mg^{2+} attraction. The former is weaker than the latter because it eventually yields catastrophically. If Glu^{386}-Asp^{197}(R) (*R* denotes that Asp^{197} belongs to the right-hand neighboring subunit) also exerts a force on helix M, then, working together, both bridges offer greater resistance to the motion demanded by the Asp^{398}-Mg^{2+} interaction than is offered by either individually, consistent qualitatively with the interpretation of Danziger et al. (29).

Interestingly, it does not appear necessary that the Asp^{155}-Arg^{395} salt-bridge break for Ile^{150} to sample the empty hydrophobic nucleotide binding cavity, as shown by the data from the *apo* run in Fig. 3 *b* in the vicinity of 15 ns. Detailed examination of the *apo* trajectory revealed that this contact arises from a short-lived fluctuation in the conformation of the Ile^{150} side chain that quickly reverted to the original conformation.

During t→r the apical domain rotates counterclockwise and the upper wing swings outward

We show in Fig. 4 *a* traces of the change in angular orientation of three selected helices, projected into the plane of the GroEL ring, versus time from the *holo* simulation: helix H and L lie in the apical domain and helix M is the major player in the closure of the binding pocket. The data indicate that the apical domain as a unit rotates in-plane between 15 and 30° counterclockwise. In Fig. 4 *b*, we show the analogous data from the *apo* simulation.

Significantly, our simulation results agree with the cryo-EM structures of **R**-state rings (16) with regard to both the direction and magnitude of rotation of the apical domains upon ATP binding, in disagreement with structures from a previous simulation study (19). Ma et al. simulated the entire **t→r** transition using targeted molecular dynamics (30), in which fictitious forces on all C_α values drove the structure from **t** to **r** in <1 ns, in effect producing a nondynamic pathway that interpolates between the endpoints. Because the net in-plane rotation of the apical domain is ~90° clockwise based on comparison of *apo* and ADP-bullet crystal structures (10), an initial 20° counterclockwise rotation of the apical domain does not appear along a targeted molecular dynamics pathway. Our simulation supports the view that the GroEL subunit naturally shifts from **t** to **r** in response to the presence of ATP in the binding pocket.

If the apical domain rotation were a strictly en bloc movement, we would expect the rotation angles of each helix, projected into the plane of the ring, to be equal. That this is not the case implies that the apical domain is deforming during the transition. This deformation is an outward opening of helices K and L, the so-called upper wing, relative to the rest of the domain. Evidence for this motion is not present in the cryo-EM structures of Ranson et al. because rigid **a**-state apical domains were fit to the electron density maps by translation/rotation only (16). There is, however, compelling evidence for such deformation of the apical domain accompanying the **T→R** transition from a definitive spectrofluorometric study (31). These workers showed that the first discernable conformational change upon rapid addition of ATP to a solution of **RR** tetradecamers occurred very quickly and was reported by increased fluorescence from the tryptophan residue mutated into position 360, normally occupied by a tyrosine. This increase in fluorescence occurs because the fluorescent side chain of the tryptophan moves away from a quenching agent, most likely the positively charged end of the side chain of Lys^{364}. Tyr^{360} and Lys^{364} are near the C-terminus of helix L, and a single turn of this helix separates them. In the **t** and **a** states, the side chain of Lys^{364} is held in intimate contact with the phenoxy ring of Tyr^{360} due to a repulsive electrostatic interaction with Arg^{284}. We observe directly in the simulation that, as the upper wing opens away, this repulsion

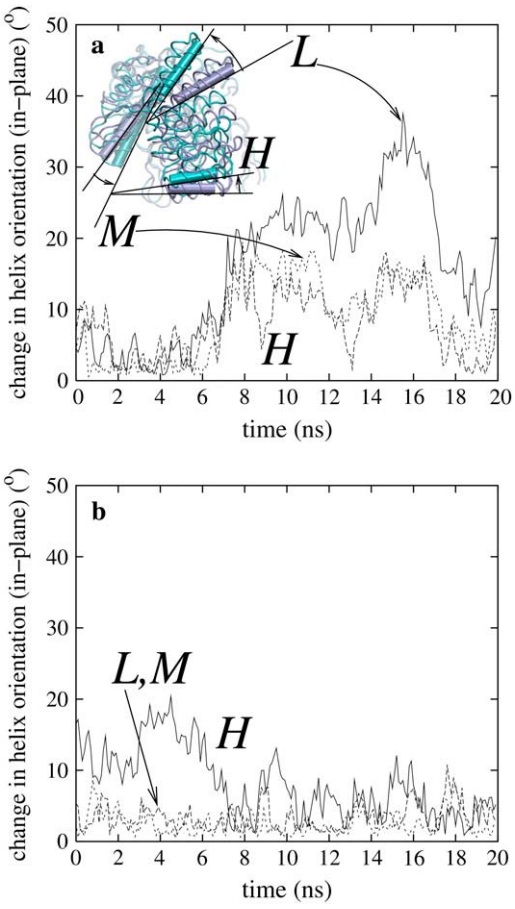

FIGURE 4 During the **t→r** transition, the apical domain rotates counterclockwise and the upper wing (helices K and L) swings away. (*a*) Change in helix orientation, projected into the GroEL ring plane, versus time for helices H, L, and M from the *holo* simulation. (*Inset*) Overlay of **t** (*gray*) and **r** (*blue*) trace structures, top view, with helices H, L, and M denoted. (*b*) Same as panel *a* for the *apo* simulation.

is relaxed and Lys^{364}'s side chain quickly moves away from the side-chain Tyr^{360} in such a way that the amino end group hydrogen-bonds to the backbone carboxyl of Tyr^{360}. It is therefore plausible that the rapid initial fluorescence observed by Cliff et al. (31) corresponds to the opening motion observed in our simulation. A similar fluorescence study with a $Lys^{368} \rightarrow$ Ala mutant could clarify this point, as Ala would not be expected to quench tryptophan fluorescence.

Structural alignments reveal broken intersubunit salt bridges but no steric clashes

Switching of intersubunit salt bridges (2,16), and, to a lesser extent, steric clashes (15,19,29) have been invoked to explain positive intra-ring cooperativity in ATP binding. To determine both the extent to which steric clashes arise and the disposition of intersubunit salt bridges when one subunit in a heptamer exists in a state different from either its left-hand or right-hand neighbor, we analyzed model trimers constructed as described in Methods. Models were constructed using average structures from our simulations replicated and aligned along equatorial domains of reference structures. We estimate the disposition of Glu^{386}-Arg^{197} intersubunit salt bridges from the C_α-C_α distances reported in Table 1. We observe that both Glu^{386}-Arg^{197} bridges are likely intact in **aaa** and **ata** trimers, and that the Glu^{386}-Arg^{197} bridge is intact in an **rt** pair, based on alignments against the *apo* structure 1XCK (26). Both appear broken when the central subunit is in the **r** state with **a** or **r** neighbors, and, interestingly, when all three subunits are in the **t** state. This suggests that what we label the **t** state is more accurately thought of as a short-lived intermediate on the *apo* $\rightarrow$ **t** transition. Indeed, Yifrach and Horovitz were the first to show that the intermediate state of any subunit in the heptamer **T** $\rightarrow$ **R** transition is **t**-like in structure but already has broken Glu^{386}-Arg^{197} salt bridges (32).

We also considered the Glu^{386}-Lys^{80} salt bridge, which has been shown to be intact for neighboring subunits in **R** state rings (16,27), and is thought to play an important role in governing positive intra-ring cooperativity because it presumably stabilizes the multisubunit **R** state. We do not observe formation of this bridge in any alignments, most likely because there is no driving force for motion of Glu^{386} toward K80 of a second subunit in our single-subunit simulations. We noted that, when any central subunit in a trimer is **r**, the Glu^{386}-Lys^{80} C_α-C_α distance is ~2.0 Å lower than in the *apo* crystal structure (data not shown).

We cannot claim to have observed breakage of the Glu^{386}-Arg^{197} bridge because we conducted a simulation of only a single subunit. We therefore cannot claim that Asp^{398}-Mg^{2+} attraction is sufficient to break both the Asp^{155}-Arg^{395} and Glu^{386}-Asp^{197}(R) bridges. We merely wished to show that the state we infer as the **r** state does indeed require that these bridges be broken, as a piece of additional evidence that the state reached by the simulation is indeed the **r** state.

No steric clashes involving atoms in the apical and/or intermediate domains are found in any trimers except those for which equatorial domains of the *cis* ring of the ADP bullet (10) were used as references. This was expected because of the slight inward tilt of the bullet equatorial domains. We disagree with previous modeling studies (15,19) regarding steric clashes. Trimers constructed by replicating average structures with equatorial domains aligned along equatorial domains in several crystal structures revealed no clashes when one subunit was in our **r** state with **t**-state or *apo* neighbors. (We note in passing that aligning a subunit from the **R** state ring of the cryo-EM structure (16) into an *apo* ring (26) also resulted in no such clashes.) This is presumably because of an important difference between clockwise and counterclockwise in-plane rotation of apical domains in a heptamer ring. Counterclockwise rotation is allowed for a single apical domain, while clockwise rotation, at least to the degree reported previously, requires concerted rotation among all seven subunits (15,19). Given that counterclockwise rotation was apparent in the cryo-EM structures of $(GroEL\text{-}ATP)_7$-$(GroEL)_7$ of Ranson et al. (16), and that counterclockwise rotation naturally occurs in the simulation, it is unlikely that concertedness among subunit transitions in the overall **T** $\rightarrow$ **R** transition has anything to do with steric clashes.

TABLE 1 C_α-C_α interatomic distances in the Glu^{386}(L)-Arg^{197}(C) (l$\rightarrow$c) and Glu^{386}(C)-Arg^{197}(R) (c$\rightarrow$r) bridges in trimers aligned against the 1XCK reference structure (26)

	Glu^{386}-Arg^{197} distances (Å)	
Trimer	l$\rightarrow$c	c$\rightarrow$r
aaa	12.4	12.4
ata	13.6	12.6
ara	15.0	14.1
ttt	14.8	14.8
trt	15.5	13.4
rrr	16.2	16.2
1XCK	*11.9*	

Quasi-harmonic analysis shows that natural modes of vibration facilitate tertiary structural changes

Because we observe a large-scale, spontaneous transition between two stable states directly, we have fully self-consistent data sets on which to test the notion that natural modes of vibrations drive conformational transitions (15). We computed all quasi-harmonic modes with frequencies of 50 cm^{-1} or lower for the **a**, **t**, and **r** states, as described in Methods. Recall that in our nomenclature, the **t** state is a state with ATP bound before closure of the pocket, while **a** denotes the strict *apo* state. Structural representations of the two lowest frequency modes in the **t** and **r** states are shown in Fig. 5.

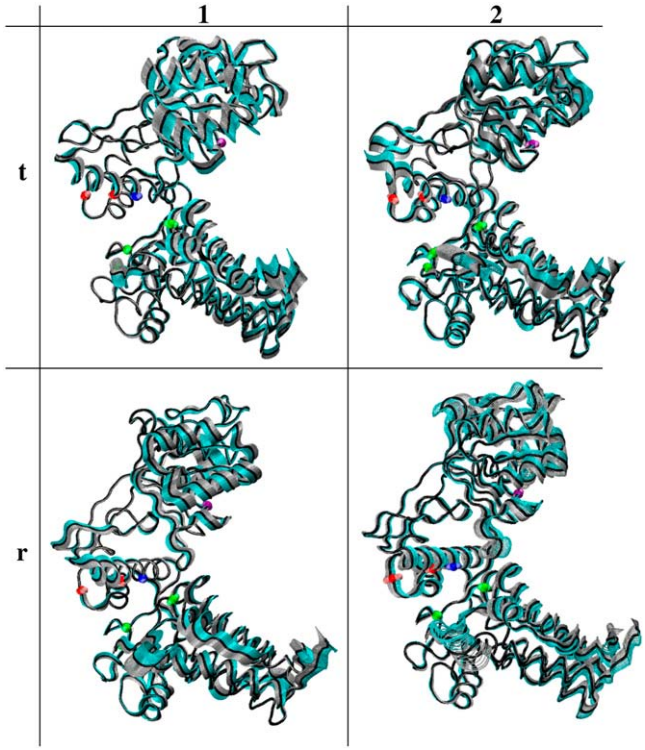

FIGURE 5 The two lowest frequency quasi-harmonic modes, labeled *1* and *2*, for the **t** and **r** state, shown in a backbone trace. The solid black trace is the average structure, and the gray and cyan traces represent displacements of positive and negative amplitude, respectively. Certain positions are highlighted with colored spheres: Asp^{155} and Arg^{395} are red, Asp^{398} is blue, binding pocket residues Pro^{33}, Ile^{493}, and Arg^{87} are green, and Arg^{197} is purple.

Mode 1 in the **t** state displays a nearly rigid intermediate domain with significant independent motion of the apical domain. In this mode, there is no motion indicating closing of the binding pocket. Mode 2 in the **t** state, however, shows pronounced vertical motion of helix M. More interesting in this mode is the concerted motion of helices M and G, guaranteed by the intact Asp^{155}-Arg^{395} salt bridge, as can be appreciated by the displacements indicated for the red spheres in the upper-right panel of Fig. 5. We note that this mode shows significant displacement of Asp^{197} in the apical domain (*purple sphere* in Fig. 5), the most of any of the four lowest frequency modes shown. This observation is consistent with the hypothesis that the Asp^{155}-Arg^{395} bridge couples the downward displacement of helix M over the binding pocket with displacement of Asp^{197}.

One should be cautious not to overinterpret the quasi-harmonic modes seen for the single subunit by extrapolating what these motions may accomplish in a complex, because the natural modes of the complex might be quite different in structure due to intersubunit contacts. However, the evidence that Asp^{155}-Arg^{395} couples motion of Arg^{197} to that of helix M is clearly demonstrated, and it reasonable to expect that similar coupling exists when a subunit is embedded in a complex. Such coupling could communicate binding pocket occupancy through the apical domain to the subunit's left-hand neighbor and help in receiving the signal that the left-hand neighbor's pocket is occupied. This leads to the larger hypothesis that concertedness in the $\mathbf{t}_7 \rightarrow \mathbf{r}_7$ transition occurs when Mg^{2+} tugging on each helix M pumps a ring-wide low-frequency vibrational mode made coherent by the Glu^{386}-Arg^{197} intersubunit bridges. We speculate that only when all seven subunits are in tune can displacements of large enough amplitude occur to effect the transition, and the complex vibrates itself through the transition. This would mean that mutation of residues involved in the network of interactions that maintains the coherence of this vibrational mode would disrupt or destroy positive cooperativity. That the Asp^{197}-$\rightarrow$Ala mutant displays no positive cooperativity (18) is consistent with this idea. Verifying this idea will require simulations of an entire seven-membered GroEL ring which may be on the cusp of feasibility today but are certainly worth pursuing.

Mode 1 in the **r** state is similar to mode 2 in the **t** state, especially with regard to motion of the intermediate and apical domains. Mode 2 in the **r** state displays much more motion of the apical domain than mode 1, and its apical motion is similar to mode 1 in the **t** state. To a significant degree, closing of the binding pocket stiffens the connection between the intermediate and apical domains, as one might expect, without greatly influencing the flexibility of the apical domain.

For all modes calculated, we evaluated the degree to which each mode contributes to displacements among the transitions in $\mathbf{a} \leftrightarrow \mathbf{t} \leftrightarrow \mathbf{r}$. Fig. 6 shows the results of this analysis in terms of the minimum mean-squared-deviation of initial structures projected along each mode relative to a target structure versus mode frequency. From this data, it is

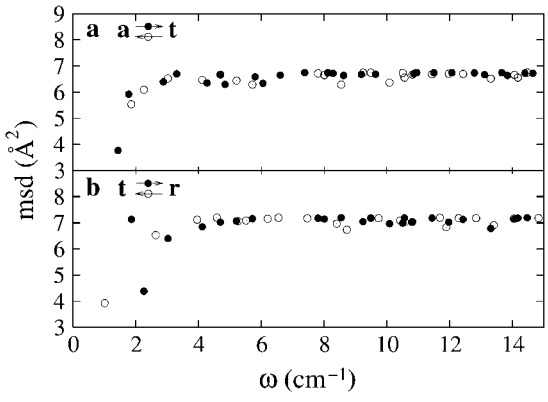

FIGURE 6 Minimum mean-squared differences between initial structures displaced along each quasi-harmonic mode and a target structure versus mode frequency. (*a*) Transition from the **a** to **t** structure and back. (*b*) Transition from the **t** to **r** structure and back.

clear that only a handful of the lowest frequency modes give rise to significant motion that facilitates transitions. The lowest-frequency mode of the **a** state clearly contributes significantly to the motion that must occur for the subunit to adopt the **t** state upon weak binding of KMgATP. The lowest frequency mode of the **t** state contributes relatively less to the motion which must occur to reattain the **a** state. ATP in the pocket has stiffened the mode that would open and close the pocket, and as a result the new lowest frequency mode is one in which the intermediate and equatorial domains move together with a rigid hinge between them and the apical domain moves more independently. Accordingly, this lowest frequency mode in the **t** state does nothing to drive motion toward the **r** state; this contribution comes mainly from the second-lowest frequency mode.

Our quasi-harmonic analyses support the original claim of Ma and Karplus (15), namely that a few of the lowest-frequency natural modes of vibration produce motion that correlates strongly to tertiary transitions. Our analysis is unique in that we have an actual spontaneous transition to which we can compare. We conclude that the natural vibrational character of the GroEL subunit facilitates the **t**→**r** transition.

Spontaneous Ala^{480} insertion into the empty nucleotide pocket inspires a new mechanism of inter-ring cooperativity

The triad Ile^{493}, Ala^{481}, and Pro^{33} define the hydrophobic part of the nucleotide pocket: Ile^{493} and Pro^{33} sandwich adenosine while Ala^{481} contacts its N6. In the *apo* simulation, after ~7 ns, we observe a shift of residues Ala^{481} and Ala^{480} that pulls Ala^{481} off the binding pocket boundary and places the methyl of Ala^{480} directly between Pro^{33} and Ile^{493} (Fig. 7). We include the distance trace between C_β of Ala^{480} and C_δ of Ile^{493} in Fig. 3 *d*. The Ala^{480} insertion remains stable for the remaining 12 ns with occasional direct contact between Pro^{33} and Ile^{493}. With Ala^{480} in this position, the accessible hydrophobic surface area owned by Pro^{33} and Ile^{493} together drops from ~100 Å^2 to 85 Å^2. This by itself would indicate hydrophobic stabilization of this configuration, but this is offset by the exposure of Ala^{481}, resulting in a negligible change in exposed hydrophobic area for this transition. Nevertheless, the arrangement of this hydrophobic area is significant, and a bound ATP, were it present, would have to shift more than one Å along its long axis to allow a clash-free contact of Ala^{481} with N6. Because Asp^{87} and Thr^{89} anchor the phosphate-side of the binding pocket, such a collapse of the pocket would likely render it incapable of accommodating ATP.

That Ala^{480} insertion occurs spontaneously in the *apo* simulation is not surprising given that the binding pocket is empty and the transition results in no significant net change in the amount of exposed hydrophobic surface area. The loop containing Ala^{480} and Ala^{481} is on the outer surface of the complex and no intersubunit interactions would easily prevent the motion of this loop that accompanies Ala^{480} insertion, suggesting this transition can occur easily in *apo* complexes. However, no *apo* crystal structure with Ala^{480} in the binding pocket has been observed, possibly because crystal forces may suppress exposure of Ala^{480} or more likely because no wild-type ATP-containing crystal structure exists. Nevertheless, it is reasonable to expect that Ala^{480} insertion competes with nucleotide binding for hydrophobic contacts with Pro^{33} and Ile^{493}, as a pocket into and out of which Ala^{480} can place its methyl spontaneously will necessarily have a lower affinity for ATP than one for which Ala^{480} remains in place below the pocket.

This leads us to suggest a novel mechanism for negative inter-ring allostery, shown schematically in Fig. 8. Ma and Karplus suppose that negative allostery requires that bound ATP in ring 1 lowers affinity for ATP in ring 2, requiring a

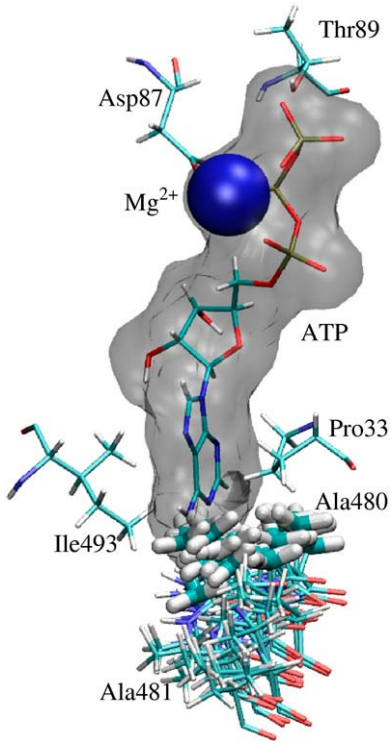

FIGURE 7 The Ala^{480} insertion transition from the *apo* simulation. Residues Ile^{493}, Pro^{33}, Asp^{87}, Thr^{89}, Ala^{480}, and Ala^{481} are rendered as rod models, and Ala^{480} and Ala^{481} are rendered in multiple snapshots between 6 and 8 ns of simulation time. The methyl side chain of Ala^{480} is rendered with thicker rods. A hypothetical ATP is shown in its crystallographic position relative to Ile^{493}, Pro^{33}, Asp^{87}, and Thr^{89}. Note that ATP is not present in the *apo* simulation; it is included here only to show that Ala^{480} occupies volume that would be occupied by ATP. A speculation on the mechanism of inter-ring cooperativity. (*a*) Select subunits in rings 1 and 2 from the *apo* crystal structure (26). (*b*) Detailed view of the inter-ring interface illustrating the important residues and motion of the proposed mechanism. The green arrow denotes force exerted by bound ATP on Ala^{480} in ring 1, which results in motion (*red arrows*) of the nearly planar (Arg^{452}-Glu^{461})$_1$-(Arg^{452}-Glu^{461})$_2$ cycle that pushes Ala^{480} into the binding pocket of ring 2. (*c*) Side view of the same configuration shown in panel *b*.

state of super low ATP affinity, designated the **t′** state (15). Here, we present a mechanism for nucleotide-depending shifting of an *apo* subunit toward the **t′** state that involves a network of steric and electrostatic interactions. Based on the most recent *apo* crystal structure of the tetradecamer (26), it was asserted that the only major inter-ring contact is the Arg^{452}-Glu^{461} salt bridge. Arg^{452} lies one turn from the C-terminus of helix P, at whose C-terminus lies Cys^{458}, which maintains a steric contact with both Ala^{480}. Glu^{461} lies at the N-terminus of helix Q and at the C-terminus of a short loop connected to Cys^{458}. As can be appreciated from the detail in Fig. 8, *b* and *c*, the $(Arg^{452}\text{-}Glu^{461})_1$-$(Arg^{452}\text{-}Glu^{461})_2$ loops form a nearly coplanar ring. We propose that the presence of ATP in the binding pocket a subunit of ring 1 forces Ala^{480}[1] into Cys^{458}[1], forcing the planar ring to rotate and shift such that Cys^{458}[2] is driven into Ala^{480}[2], a change in conformation that shifts the equilibrium in the *apo* subunit toward an Ala^{480}-filled binding pocket.

This mechanism, although it is purely speculative, was inspired by the observation from the MD simulation that the loop containing Ala^{481} and Ala^{480} was flexible enough to allow spontaneous insertion of Ala^{480} into the nucleotide pocket, thereby producing an ostensibly **t′** state. To establish whether this mechanism is valid will require mutational studies not yet attempted. For example, an $Ala^{480}\rightarrow$Gly mutant may prevent this transition, but may also alter the conformational flexibility of the backbone around position 480 which itself may alter the structure and affinity of the binding pocket. A residue with a larger side chain than alanine's, perhaps phenylalanine or tryptophan, which can form the floor of the binding pocket without easily inserting between Pro^{33} and Ile^{493}, may also be an interesting choice for mutation into position 480. Finally, because the relatively large sulfur atom on Cys^{458} allows direct steric contact with the methyl group of Ala^{480}, a $Cys^{458}\rightarrow$Gly mutant may also suffer a disrupted inter-ring communication network.

Bartolucci et al. also proposed a mechanism for negative cooperativity based on a comparison of their *apo* crystal structure and that of the ADP bullet (26). This mechanism relies on a much more spatially extensive network of interactions than that presented here, but it has the apparent advantage that it potentially explains why the $Arg^{13}\rightarrow$Ala mutant has reduced inter-ring cooperativity (33). We submit that an intact Arg^{13}-Glu^{518} salt bridge rigidifies the equatorial domain and thereby allows more focused transmission of force from Ala^{480} to Cys^{458}, primarily because helix A, at whose N-terminus lies Pro^{33}, would be less flexible. In the $Arg^{13}\rightarrow$Ala mutant, no such bridge can form, and helix A is free to shift axially away from the binding pocket due to thermal noise, which might make Ala^{480} less able to form stable hydrophobic contacts with both Pro^{33} and Ile^{493} than is the adenosine of an ATP ligand, thus shifting equilibrium away from the **t′** state and reducing inter-ring cooperativity.

CONCLUSIONS

We are the first to show that the **t**→**r** transition in an isolated GroEL subunit occurs in an unbiased molecular dynamics simulation without the need to drive the structure toward a target. The simulations unambiguously show that the presence of KMgATP in the binding pocket causes this transition chiefly due to a strong interaction between the Mg^{2+} of the ATP and Asp^{398}. Counterclockwise apical domain rotation in agreement with that inferred from cryoelectron microscopy structures (16) is observed. An important aspect of our work is that we show that the flexibility and forces required to effect the **t**→**r** transition are encoded in the subunit sequence and do not depend upon interactions in the complex. As pointed out by Ma and Karplus (15), this indicates that the **T**→**R** transition in a GroEL ring is better thought of as coupled tertiary changes rather than concerted changes in quaternary structure. Based

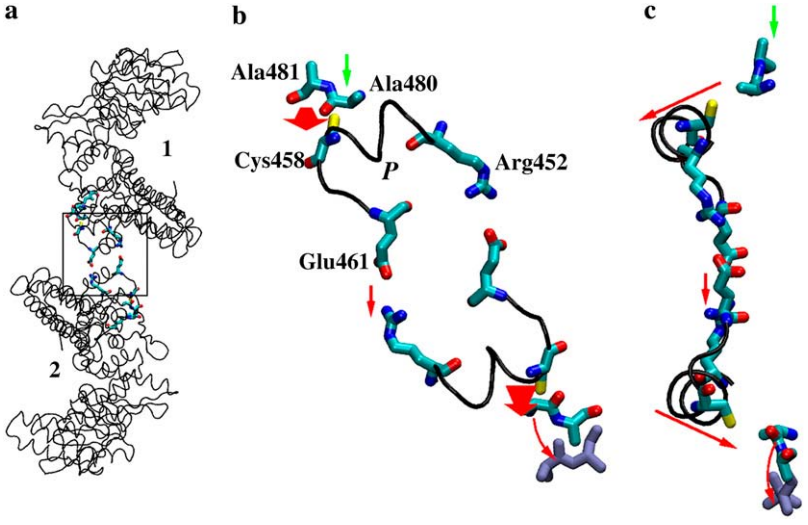

FIGURE 8 A speculation on the mechanism of inter-ring cooperativity. (*a*) Select subunits in ring 1 and 2 from the *apo* crystal structure (26). (*b*) Detailed view of the inter-ring interface illustrating the important residues and motion of the proposed mechanism. The green arrow denotes force exerted by bound ATP on Ala^{480} in ring 1, which results in motion (*red arrows*) of the nearly planar $(Arg^{452}\text{-}Glu^{461})_1$-$(Arg^{452}\text{-}Glu^{461})_2$ cycle that pushes Ala^{480} into the binding pocket of ring 2. (*c*) Side view of the same configuration shown in panel *b*.

on model trimers, no intersubunit steric clashes arise during the $\mathbf{t} \rightarrow \mathbf{r}$ transition. Quasi-harmonic modes of vibration clearly facilitate the transition. We are also the first to observe the spontaneous insertion of Ala^{480} into the empty nucleotide pocket, a transition that may give rise to the super-low ATP-affinity $\mathbf{t}'$ state, and we postulated a testable mechanism of inter-ring negative cooperativity in ATP binding that relies on this transition.

GroEL is a fascinating protein: it is a machine that drives substrate proteins toward folded conformations with a mechanism that relies on the directionality of ATP binding and hydrolysis as well as strongly interconnected positive and negative cooperativity to regulate affinities. Though we have focused on only one subunit in the complete tetradecamer/co-chaperonin/substrate system, the behavior we observe in the unbiased simulation sheds new light on the dynamics of GroEL's mechanism and certainly provide new ideas to pursue in explaining its behavior. It is particularly surprising and encouraging that such a large-scale allosteric transition is directly observable in an unbiased, all-atom molecular dynamics simulation.

We thank Prof. A. Horovitz for stimulating discussion and a critique of the manuscript.

We acknowledge the National Science Foundation for financial support through grant No. DMR-6427643.

REFERENCES

1. Sigler, P. B., Z. Xu, H. S. Rye, S. G. Burston, W. A. Fenton, and A. L. Horwich. 1998. Structure and function in GroEL-mediated protein folding. *Annu. Rev. Biochem.* 67:581–608.
2. Horwich, A. L., F. W. Farr, and W. A. Fenton. 2006. GroEL-GroES-mediated protein folding. *Chem. Rev.* 106:1917–1930.
3. Hohn, T., B. Hohn, A. Engel, M. Wurtz, and P. R. Smith. 1979. Isolation and characterization of the host protein groE involved in bacteriophage λ-assembly. *J. Mol. Biol.* 129:359–373.
4. Hendrix, R. W. 1979. Purification and properties of groE, a host protein involved in bacteriophage assembly. *J. Mol. Biol.* 129:375–392.
5. Hunt, J. F., A. J. Weaver, S. J. Landry, L. Gierasch, and J. Deisenhofer. 1996. The crystal structure of the GroES co-chaperonin at 2.8 Å resolution. *Nature.* 379:37–45.
6. Gray, T. E., and A. R. Fersht. 1991. Cooperativity in ATP hydrolysis by GroEL is increased by GroES. *FEBS Lett.* 292:254–258.
7. Inobe, T., T. Makio, E. Takasu-Ishikawa, T. P. Terada, and K. Kuwajima. 2001. Nucleotide binding to the chaperonin GroEL: non-cooperative binding of ATP analogs and ADP, and cooperative effect of ATP. *Biochim. Biophys. Acta.* 1545:160–173.
8. Yifrach, O., and A. Horovitz. 1995. Nested cooperativity in the ATPase activity of the oligomeric chaperonin GroEL. *Biochemistry.* 34:5303–5308.
9. Bochkareva, E. S., N. M. Lissin, G. C. Flynn, J. E. Rothman, and A. S. Girshovich. 1992. Positive cooperativity in the functioning of molecular chaperone GroEL. *J. Biol. Chem.* 267:6796–6800.
10. Xu, Z., A. L. Horwich, and P. B. Sigler. 1997. The crystal structure of the asymmetric GroEL-GroES-$(ADP)_7$ chaperonin complex. *Nature.* 388:741–750.
11. Fenton, W. A., J. S. Weissman, and A. L. Horwich. 1996. Putting a lid on protein folding: structure and function of the co-chaperonin, GroES. *Chem. Biol.* 3:157–161.
12. Braig, K., Z. Otwinovski, R. Hedge, D. C. Boisvert, A. Joachimiak, A. L. Horwich, and P. B. Sigler. 1994. The crystal structure of bacterial chaperonin GroEL at 2.8 Å. *Nature.* 371:578–586.
13. Boisvert, D. C., J. Wang, Z. Otwinowski, A. L. Horwich, and P. B. Sigler. 1996. The 2.4 Å crystal structure of the bacterial chaperonin GroEL complexed with $ATP_\gamma S$. *Nat. Struct. Biol.* 3:170–177.
14. Fenton, W. A., Y. Kashi, K. Furtak, and A. L. Horwich. 1994. Residues in chaperonin GroEL required for polypeptide binding and release. *Nature.* 371:614–619.
15. Ma, J., and M. Karplus. 1998. The allosteric mechanism of the chaperonin GroEL: a dynamic analysis. *Proc. Natl. Acad. Sci. USA.* 95:8502–8507.
16. Ranson, N. A., G. W. Farr, A. M. Rosenman, B. Gowen, W. A. Fenton, A. L. Horwich, and H. R. Saibil. 2001. ATP-bound states of GroEL captured by cryo-electron microscopy. *Cell.* 107:869–879.
17. Wang, J., and D. C. Boisvert. 2003. Structural basis for GroEL-assisted protein folding from the crystal structure of $(GroEL\text{-}KMgATP)_{14}$ at 2.0 Å resolution. *J. Mol. Biol.* 327:843–855.
18. Yifrach, O., and A. Horovitz. 1994. Two lines of allosteric communication in the oligomeric chaperonin GroEL are revealed by the single mutation $Arg^{196} \rightarrow$ Ala. *J. Mol. Biol.* 243:397–401.
19. Ma, J., P. B. Sigler, Z. Xu, and M. Karplus. 2000. A dynamic model for the allosteric mechanism of GroEL. *J. Mol. Biol.* 302:303–313.
20. Hyeon, C., G. H. Lorimer, and D. Thirumalai. 2006. Dynamics of allosteric transitions in GroEL. *Proc. Natl. Acad. Sci. USA.* 103:18939–18944.
21. White, H. E., S. Chena, A. M. Roseman, O. Yifrach, A. Horovitz, and H. R. Saibil. 1997. Structural basis of allosteric changes in the GroEL mutant $Arg^{197} \rightarrow$ A. *Nat. Struct. Biol.* 4:690–694.
22. Kalé, L., R. Skeel, M. Bhandarkar, R. Brunner, A. Gursoy, N. Krawetz, J. Phillips, A. Shinozaki, K. Varadarajan, and K. Schulten. 1999. NAMD2: greater scalability for parallel molecular dynamics. *J. Comput. Phys.* 151:283–312.
23. MacKerell, Jr., A. D., D. Bashford, M. Bellott, R. L. Dunbrack, Jr., J. D. Evanseck, M. J. Field, S. Fischer, J. Gao, H. Guo, S. Ha, D. Joseph-McCarthy, L. Kuchnir, K. Kuczera, F. K. Lau, C. Mattos, S. Michnick, T. Ngo, D. T. Nguyen, B. Prodhom, W. E. R. Koeppe III, B. Roux, M. Schlenkrich, J. C. Smith, R. Stote, J. Straub, M. Watanabe, J. Wiórkiewicz-Kuczera, D. Yin, and M. Karplus. 1998. All-atom empirical potential for molecular modeling and dynamics studies of proteins. *J. Phys. Chem. B.* 102:3586–3616.
24. Follope, N., and A. D. MacKerell, Jr. 2000. All-atom empirical force field for nucleic acids. I. Parameter optimization based on small molecule and condensed phase macromolecular target data. *J. Comput. Chem.* 21:86–104.
25. MacKerell, A. D., Jr., and N. K. Banavali. 2000. All-atom empirical force field for nucleic acids. II. Application to molecular dynamics simulations of DNA and RNA in solution. *J. Comput. Chem.* 21:105–120.
26. Bartolucci, C., D. Lamba, S. Grazulis, E. Manakova, and H. Heumann. 2005. Crystal structure of wild-type chaperonin GroEL. *J. Mol. Biol.* 354:940–951.
27. Ranson, N. A., D. K. Clare, G. W. Farr, D. Houldershaw, A. L. Horwich, and H. R. Saibil. 2006. Allosteric signaling of ATP hydrolysis in GroEL-GroES complexes. *Nat. Struct. Mol. Biol.* 13:147–152.
28. Pearlman, D. A., D. A. Case, J. W. Caldwell, W. Ross, I. T. E. Cheatham, S. DeBolt, D. Ferguson, G. Seibel, and P. Kollman. 1995. AMBER, a package of computer programs for applying molecular mechanics, normal mode analysis, molecular dynamics and free energy calculations to simulate the structural and energetic properties of molecules. *Comput. Phys. Comm.* 91:1–41.
29. Danziger, O., D. Rivenzon-Segal, S. G. Wolf, and A. Horowitz. 2003. Conversion of the allosteric transition of GroEL from concerted to sequential by the single mutation $Asp\text{-}^{155} \rightarrow$ Ala. *Proc. Natl. Acad. Sci. USA.* 100:13797–13802.
30. Schlitter, J., M. Engels, P. Kruger, E. U. Jacoby, and W. Wollmer. 1993. Targeted molecular dynamics simulation of conformational change: application to the T-R transition in insulin. *Mol. Sim.* 10:291–308.

31. Cliff, M. J., N. M. Kad, N. Hay, P. A. Lund, M. R. Webb, S. G. Burston, and A. R. Clarke. 1999. A kinetic analysis of the nucleotide-induced allosteric transitions of GroEL. *J. Mol. Biol.* 293: 667–684.

32. Yifrach, O., and A. Horovitz. 1998. Mapping the transition state of the allosteric pathway of GroEL by protein engineering. *J. Am. Chem. Soc.* 120:13262–13263.

33. Aharoni, A., and A. Horovitz. 1996. Inter-ring communication is disrupted in the GroEL mutant $Arg^{13} \rightarrow Gly$; $Ala^{126} \rightarrow Val$ with known crystal structure. *J. Mol. Biol.* 258:732–735.

34. Humphrey, W., A. Dalke, and K. Schulten. 1996. VMD—visual molecular dynamics. *J. Mol. Graph.* 14:33–38.

35. Frishman, D., and P. Argos. 1995. Knowledge-based protein secondary structure assignment. *Proteins.* 23:566–579.